Supplementary file

In-situ hydrogen production from natural gas reservoirs and gas separation by graphite packing: Process simulation and experimental study

Bennet Nii Tackie-Otoo¹, Mohamed Mahmoud^{1*}, Arshad Raza^{1*}, Shirish Patil¹, Mobeen Murtaza², Muhammad Shahzad Kamal², Umer Zahid^{3,4}

¹Department of Petroleum Engineering, King Fahd University of Petroleum & Minerals (KFUPM), Dhahran 31261, Saudi Arabia

²Center for Integrative Petroleum Research (CIPR), King Fahd University of Petroleum & Minerals (KFUPM),

Dhahran 31261, Saudi Arabia

³Department of Chemical Engineering, King Fahd University of Petroleum and Minerals, Dhahran 31261, Saudi Arabia

⁴Interdisciplinary Research Center for Membranes & Water Security, King Fahd University of Petroleum & Minerals, Dhahran 31261, Saudi Arabia

E-mail address: bennetnii.tackieotoo@kfupm.edu.sa (B. N. Tackie-Otoo); mmahmoud@kfupm.edu.sa (M. Mahmoud); arshad.raza@kfupm.edu.sa (A. Raza); patil@kfupm.edu.sa (S. Patil); mobeen@kfupm.edu.sa (M. Murtaza); shahzadmalik@kfupm.edu.sa (M. S. Kamal); uzahid@kfupm.edu.sa (U. Zahid).

* Corresponding author (ORCID: 0000-0002-4395-9567 (M. Mahmoud); 0000-0001-7706-1002 (A. Raza))

Tackie-Otoo, B. N., Mahmoud, M., Raza, A., Patil, S., Murtaza, M., Kamal, M. S., Zahid, U. In-situ hydrogen

production from natural gas reservoirs and gas separation by graphite packing: Process simulation and

experimental study. Advances in Geo-Energy Research, 2025, 18(2): 165-179.

The link to this file is: https://doi.org/10.46690/ager.2025.11.06

Supplementary A: Review

A1. Review of studies on ISCG of heavy oil

Previously reported H₂ generation during field-scale operations confirmed the feasibility of ISCG. These operations include *in-situ* combustion (ISC) and Toe-to-Heel Air Injection (THAI), as reported by Ifticene et al. (2023) and summarized in Table A1. Consequently, several studies investigated adapting traditional ISC techniques, initially developed for heavy oil and bitumen recovery, for hydrogen production through gasification (Afanasev et al., 2023; Askarova et al., 2023; He et al., 2023; Song et al., 2024). The contributions of these studies are summarized in Table 2.

Table A1: Research advances on IHP via ISCG.

Reference	Novelties	Study type	Major Findings
Kapadia et al. (2011)	Proposed a new kinetic model to predict hydrogen generation from Athabasca bitumen via <i>in-situ</i> combustion and validated it with literature data.	Simulation	 The proposed reaction scheme effectively represents hydrogen generation from Athabasca bitumen. Hydrogen yield is maximized at 320-380 °C and 4 MPa. Dominance of thermal cracking and low-temperature oxidation promotes coke formation, enabling hydrogen production via gasification.
Kapadia et al. (2013)	Proposed a field-scale <i>in-situ</i> bitumen gasification process with steam and oxygen injection, enhancing hydrogen yield and efficiency while lowering water use and emissions compared to Steam-Assisted Gravity Drainage (SAGD).	Simulation	 The proposed reaction scheme aligned well with field data from the Marguerite Lake ISC pilot. Cyclic steam and oxygen injection produced hydrogen, methane, CO, and CO₂ along with bitumen, though oil yield was lower than in SAGD. CO₂ emissions per unit of energy were slightly lower than those from a conventional SAGD process.
He et al. (2023)	Pioneers the use of ramped temperature oxidation (RTO) experiments to quantitatively analyze hydrogen generation mechanisms from heavy oil gasification.	Experimental	 Reservoir core samples outperformed sand models in hydrogen generation, likely due to mineral catalysis and complex pore structures. Crude oil produced hydrogen at lower temperatures (500-550 °C) than carbon (700-750 °C). Hydrogen generation mainly occurred via coke gasification and water-gas shift reactions, with heavy oil yielding more hydrogen than light oil.
Askarova et al. (2023)	Introduces a novel method for <i>in-situ</i> catalytic methane conversion within gas reservoirs, using ISC of oil to create the necessary high-temperature environment.	Experimental and simulation	 Methane can be converted to hydrogen in gas reservoirs via <i>in-situ</i> combustion of residual oil, with up to 40% conversion. Actual hydrogen yield was lower due to secondary hydrogen-consuming reactions. Heavy oil was significantly upgraded, producing lighter oil with reduced density, viscosity, sulfur, and asphaltenes.

Table A1 continued

Reference	Novelties	Study type	Major Findings	
Ikpeka & Ugwu (2023)	Developed a combustion-based model with four hydrogen-producing reactions for simulating <i>in-situ</i> hydrogen production, validated by thermal simulation.	Simulation	 Hydrogen yield shows an upward sinusoidal trend with increasing steam-carbon ratio. Hydrogen yield decreases sinusoidally with higher oxygen-carbon ratio due to hydrogen re-oxidation into steam. 	
Afanasev et al. (2023)	Demonstrated catalytic enhancement of cyclic steam-air stimulation for simultaneous <i>in-situ</i> hydrogen generation and heavy oil upgrading using a dualporosity reservoir model.	Experimental	 Two ISC cycles were successfully simulated, with forward combustion reaching 550-600 °C. Oil recovery was 95%, and produced oil was slightly upgraded in density (0.942 to 0.933 g/mL). <i>In-situ</i> hydrogen generation was confirmed, mainly via oil thermal cracking, yielding 2.10 L of H₂. 	
Song et al. (2023)	Performed numerical simulations of ISCG, achieving up to 28 mol.% hydrogen from bitumen and highlighting the critical roles of temperature and oxygen concentration	Simulation	 Up to 28% hydrogen mole fraction was achieved during ISCG at 735 °C, 4 MPa, and 0.18% fluid volume fraction. Hydrogen formation is dominated by the water-gas shift reaction above 665 °C and by coke gasification below 500 °C. Water content in injected fluids strongly influences H₂ and CO₂ yields, with 0.18% volume fraction being optimal. 	
Pu et al. (2023)	Demonstrated catalytic enhancement of cyclic steam-air stimulation for simultaneous <i>in-situ</i> hydrogen generation and heavy oil upgrading using a dualporosity reservoir model.	Experimental	 Raising temperature from 300 to 600 °C boosts hydrogen yield (3.25% to 18.75%) and conversion efficiency (0.22 to 17.21 mg/g via enhanced water-gas shift and steam reforming. Hydrogen fraction rises then falls with longer reaction times due to declining CO generation. Metallic oxides and debris catalyze hydrogen production; CaO he reduce CO₂ through calcification. Lower oil/water ratios favor hydrogen generation, making water-depleted reservoirs (e.g., post-SAGD) suitable for <i>in-situ</i> H₂ production. 	
Song et al. (2024)	Developed a lab-scale ISCG simulation achieving 34 mol.% hydrogen at 800°C, highlighting temperature and water as key factors.	Simulation	 Hydrogen concentrations up to 34 mol% were achieved at ~800 °C. Key factors influencing hydrogen generation included injection temperature, O₂/N₂ ratio, injection rate, water, and oil fractions. Strong interactions were observed between oxygen ratio, water content, and temperature. 	

A2. Review of studies on H₂/CO₂ diffusion and adsorption in graphite

Various studies have shown the gas separation capability of graphite through diffusion and adsorption as summarized in Table A2. Across simulations and experiments, CO₂ shows stronger adsorption on graphite than H₂, with higher binding energies and slower diffusion. H₂, however, diffuses more rapidly: an advantageous contrast for separation (Bartolomei & Giorgi, 2016; Mishra & Ramaprabhu, 2010; Trinh et al., 2013). However, as reported by Trinh et al. (2013), at higher temperatures, CO₂/H₂ adsorption selectivity decreases as H₂ flux rises, revealing a trade-off between uptake and permeability. Graphite-based membranes demonstrate promising H₂/CO₂ selectivity under ideal, single-gas conditions, yet real-mixture separations are much lower, underlining the challenge of translating ideal performance to practical environments (Schulz et al., 2014). A consistent observation across multiple permeation studies is that H₂ transport is dominated by molecular flow through porosity rather than lattice diffusion, with flux scaling linearly with pressure and inversely with thickness (Schneider et al., 2007; Spitsyn et al., 2007, 2009). Nevertheless, permeabilities vary by orders of magnitude across graphite grades, showing that microstructural control is critical for reproducibility (Spitsyn et al., 2009). Trapping energetics further complicate transport: distinct sites at ~2.6 eV and ~4.4 eV govern hydrogen retention and release, influencing transient behavior and isotope management (Atsumi & Tauchi, 2003).

Table A2: Overview of studies on graphite materials for gas separation and hydrogen transport.

Reference	Summary	Mechanism focus	Main findings
Bartolomei & Giorgi (2016)	A novel nanoporous graphite based on graphynes shows high propensity for CO ₂ physisorption compared to other gases.	Adsorption	 The novel nanoporous graphite based on graphynes sheets shows a high propensity for CO₂ physisorption with a binding energy of about 200 meV. The adsorption enthalpy for CO₂ is significantly higher than for other gases like N₂, H₂O, and H₂, indicating strong physisorption. The material is proposed as an efficient adsorbing medium for both pre- and post-combustion carbon capture processes with a high gravimetric storage capacity.
Schulz et al. (2014)	Pressed graphite membranes enable fast, selective H ₂ permeation via aligned flake structures, outperforming molecular sieves in ethanol steam reforming.	Membrane separation	 The pressed graphite membrane showed a real mixture separation factor of around 5 for H₂/CO₂, despite a higher ideal separation factor. The membrane was hydrogen-selective at temperatures between 100 and 250°C, with specific separation factors for H₂/CO₂ and H₂/H₂O. The hydrogen permeability of the pressed graphite membranes was significantly higher than that of molecular sieve membranes, and they are practical for use due to their ease of preparation and low cost.
Trinh et al. (2013)	Molecular dynamics simulations show CO ₂ has higher adsorption and lower self-diffusion on graphite compared to H ₂ , suggesting graphite can be used for CO ₂ enrichment.	Adsorption Diffusion	 The binding energy of CO₂ on graphite is three times larger than that of H₂, indicating stronger interaction. Selectivity of CO₂ over H₂ is five times larger at lower temperatures than at higher temperatures. The self-diffusion coefficient of CO₂ is smaller than that of H₂, with CO₂ having a higher energy barrier for diffusion.
Mishra & Ramaprabhu (2010)	The study develops functionalized graphite nanoplatelets as low-cost CO ₂ adsorbents, showing high uptake under varying high-pressure conditions.	Adsorption	 Maximum adsorption capacities of 0.0036, 0.004, and 0.0049 mol/g were observed at 1.2 MPa equilibrium pressure and at 100, 50, and 25 °C temperatures respectively. The adsorption mechanism involves interaction with functional groups and gas condensation rather than micropore filling. f-GNP can be used as a CO2 adsorbent under high-pressure conditions and can be reused by desorbing CO2 at 150°C under vacuum.

Table A2 continued

Reference	Summary	Mechanism focus	Main findings
Spitsyn et al. (2009)	The study investigates hydrogen permeation in fine-grain graphite (MPG-8, R5710) and CFC (NB31) using gas-driven permeation experiments, revealing transport through internal porosity, with MPG-8 and NB31 showing high permeability and R5710 significantly lower.	Diffusion/Permeation	 The gas-driven hydrogen isotopes permeation through carbon materials occurs through internal porosity rather than atomic diffusion. The permeability of MPG-8 and Nb31 is of the same order, while R5710 has a permeability two orders of magnitude less due to differences in porosity and void size. The permeability of carbon-based materials strongly depends on their structure, influencing deep diffusion and trapping of deuterium.
Schneider et al. (2007)	The study employs dynamic Monte Carlo simulations to analyze hydrogen isotope transport in porous graphite, highlighting void effects on re-emission and extending models to include molecular species.	Diffusion/Permeation (modeling)	 The simulation results agree with experimental trends showing hydrogen re-emission in molecular form at lower temperatures and atomic form at higher temperatures. Increasing the void fraction in graphite leads to an increase in hydrogen molecule re-emission. The model results for isotope exchange agree with experimental relative fluxes but show a discrepancy in time-dependent behavior.
Spitsyn et al. (2007)	The study measures hydrogen permeation through fine-grain graphite MPG-8.	Diffusion/Permeation	 The permeation rate of hydrogen through fine-grain graphite MPG-8 is proportional to gas pressure and inversely proportional to thickness, indicating gas flow through internal porosity. The specific bulk conductivity of the graphite is measured to be about (5-7.3) × 10¹⁵ molecules·s⁻¹·m⁻¹·Pa⁻¹. Surface treatments have a minimal impact on permeation rates, with most resulting in less than a 10% change.
Atsumi & Tauchi (2003)	The study identifies two hydrogen trapping sites in graphite: edge surface (2.6 eV) and internal crystallite (4.4 eV), with the latter primarily governing hydrogen retention.	Diffusion/Trapping	 Hydrogen absorption and transport in graphite materials were studied for fusion reactor and hydrogen storage applications. Two types of hydrogen trapping sites were identified: Traps 1 with an enthalpy of 4.4 eV and Traps 2 with an enthalpy of 2.6 eV. Traps 2 dominate hydrogen retention in usual graphite samples and show pressure-dependent retention due to equilibrium processes.

Supplementary B: Process simulation

B1. Gibbs free energy minimization

The total Gibbs free energy (G^i) is defined as the summation of the product of the number of moles (n) and the chemical potential (μ) for each reacting species (i) (Okoji et al., 2024):

$$G^t = \sum_{i=1}^n n_i \mu_i \tag{B1}$$

This model requires process parameters such as the temperature and pressure, initial reacting mixture composition, chemical compounds involved in the process and expressions that define the thermodynamic potential of the various species (Żogała, 2014). As detailed by Żogała (2014) the chemical potential μ_i is expressed as a function of the standard Gibbs free energy of formation at 298 K ($\Delta_R G_{i,298}^o$) and the species' mole fraction (x_i):

$$\mu_i = \Delta_R G^{\circ}_{i,298} + RT \ln(x_i) \tag{B2}$$

where R is the universal gas constant (8.314 J/mol K) and T is absolute temperature (K). Substituting this into the total Gibbs energy equation gives:

$$G^{t} = \sum_{i=1}^{n} n_{i} \Delta_{R} G^{\circ}_{i,298} + \sum_{i=1}^{n} n_{i} RT \ln\left(\frac{n_{i}}{n}\right)$$
(B3)

To ensure elemental conservation during minimization, atom balance constraints are imposed, where the number of atoms of each element across all species must equal the total input quantity:

$$\sum_{i=1}^{N} a_{ij} n_i = A_j \tag{B4}$$

where a_{ij} denotes the number of atoms of element j in species i, and A_j is the total number of atoms of element j present initially. The minimization of Gibbs free energy subject to these constraints is carried out using the method of Lagrange multipliers (λ_i). The resulting Lagrangian function (L) is:

$$L = G^{t} - \sum_{i=1}^{k} \lambda_{j} \left(\sum_{i=1}^{N} a_{ij} n_{j} - A_{j} \right)$$
 (B5)

Solving the system of equations derived from setting the partial derivatives of this function with respect to each mole quantity to zero yields the equilibrium composition of the reacting mixture.

B2. Expression of rate equations for SMR

The reaction rate expressions as given by Xu & Froment (1989):

$$r_{1} = \frac{\frac{k_{1}}{p_{H_{2}}^{2.5}} \left[p_{CH_{4}} p_{H_{2}O} - \frac{p_{H_{2}}^{3} p_{CO}}{K_{1}} \right]}{DEN^{2}}$$
(B6)

$$r_2 = \frac{\frac{k_2}{p_{H_2}} \left[p_{CO} p_{H_2O} - \frac{p_{H_2} p_{CO_2}}{K_2} \right]}{DEN^2}$$
 (B7)

$$r_3 = \frac{\frac{k_3}{p_{H_2}^{3.5}} \left[p_{CH_4} p_{H_2O}^2 - \frac{p_{H_2}^4 p_{CO_2}}{K_3} \right]}{DEN^2}$$
 (B8)

$$DEN = 1 + K_{CO}p_{CO} + K_{H_2}p_{H_2} + K_{CH_4}p_{CH_4} + \frac{K_{H_2O}p_{H_2O}}{P_{H_2}}$$
(B9)

The reaction rate expressions as given by Hou & Hughes (2001):

$$r_{1} = \frac{\frac{k_{1}}{p_{H_{2}}^{1.25}} \left[p_{CH_{4}} p_{H_{2}O}^{0.5} - \frac{p_{H_{2}}^{3} p_{CO}}{K_{1} p_{H_{2}O}^{0.5}} \right]}{den^{2}}$$
(B10)

$$r_{2} = \frac{\frac{k_{2}}{p_{H_{2}}^{0.5}} \left[p_{CO} p_{H_{2}O}^{0.5} - \frac{p_{H_{2}} p_{CO_{2}}}{K_{2} p_{H_{2}O}^{0.5}} \right]}{den^{2}}$$
(B11)

$$r_{3} = \frac{\frac{k_{3}}{p_{H_{2}}^{1.75}} \left[p_{CH_{4}} p_{H_{2}O} - \frac{p_{H_{2}}^{4} p_{CO_{2}}}{K_{2} p_{H_{2}O}} \right]}{den^{2}}$$
(B12)

$$den = 1 + K_{CO}p_{CO} + K_{H_2}p_{H_2}^{0.5} + \frac{K_{H_2O}p_{H_2O}}{p_{H_2}}$$
(B13)

In the above expressions, r_n , k_n and K_n are the reaction rate, rate constant and equilibrium constant for the reversible reaction n respectively. DEN/den represent the adsorption term presented by the various authors, p_i denotes the partial pressure of component i, while K_i represents its corresponding adsorption equilibrium constant.

In ASPEN Plus, the above rate equations are generally expressed as (Al-Malah, 2022):

$$r = \frac{F_k \times d_f}{DEN} \tag{B14}$$

where F_k is the kinetic factor and d_f is the driving force. The kinetic factor, when a reference temperature T_0 is specified is expressed as:

$$F_k = k \left(\frac{T}{T_0}\right)^n e^{-\left(\frac{E}{R}\right)\left(\frac{1}{T} - \frac{1}{T_0}\right)}$$
 (B15)

when no reference temperature is specified:

$$F_k = kT^n e^{-\frac{E}{RT}} \tag{B16}$$

This factor accounts for the dependence of the reaction rate on temperature. It combines the Arrhenius behavior $(e^{-E/RT})$ and temperature dependence correction $(T^n \text{ or } (T/T_0)^n)$. k is the pre-exponential factor

(frequency factor), T is absolute temperature (K), E is activation energy (J/mol), n is temperature exponent, and R is the universal gas constant (8.314 J/mol K). The driving force is expressed as:

$$d_f = K_1 \prod_i C_i^{v_i} - K_2 \prod_j C_j^{v_j}$$
 (B17)

This expression represents the difference in chemical potential between the forward and reverse reactions. It defines the net driving force that determines the direction and extent of the reaction. K_I and K_2 are the equilibrium constants for the forward and reverse reaction respectively. C_i and C_j are the concentrations (or partial pressures) of reactants and products while v_i and v_j are the stoichiometric coefficients for the respective species. The adsorption term is expressed as:

$$DEN = \left[\sum_{i=1}^{n} K_i \left(\prod_j C_j^{v_j} \right) \right]^m \tag{B18}$$

This term describes the effects of reactant adsorption on the overall reaction rate. K_i is the adsorption equilibrium constant for species i. C_j represents the concentration (or partial pressure) of species j and v_j is the corresponding stoichiometric or empirical exponent while m is the adsorption expression exponent.

B3. Tables for process simulation

Table B1: Natural gas reservoir compositions (Roussanaly et al., 2014).

Composition	Mole fraction (x _i)					
	Groningen (Netherlands)	Ardjuna (Indonesia)	Uthmaniyah (Saudi Arabia)	Lacq (France)	Uch (Pakistan)	
Methane	0.813	0.657	0.555	0.69	0.273	
Ethane	0.029	0.085	0.18	0.03	0.007	
Propane	0.004	0.145	0.098	0.009	0.003	
Butane	0.001	0.051	0.045	0.005	0.003	
pentane	0.001	0.008	0.016	0.005	0.000	
Hexane	0.000	0.000	0.000	0.000	0.000	
CO ₂	0.009	0.041	0.089	0.093	0.462	
N ₂	0.143	0.013	0.002	0.015	0.252	
H ₂ S	0.000	0.000	0.015	0.153	0.000	

Table B2: Kinetic parameters for SMR and WGS over Ni-based catalyst supported on alumina.

Rate constant or	Xu and Froment (19	89)	Hou and Hughes (2001)		
equilibrium constant	Pre-exponential factor	Ea (J/mol)	Pre-exponential factor	Ea (J/mol)	
\mathbf{k}_1	$3.74E+14 \text{ mol } (N/m^2)^{0.5}/g \text{ s}$	240100	3.33E+09 mol (N/m ²) ^{0.25} /g s	209200	
k_2	5.37E-03 mol/g s N/m ²	67130	6.03E-01 mol N/m ² /g s	15400	
k_3	8.95E+13 mol (N/m ²) ^{0.5} /g s	243900	6.15E+03 mol (N/m ²) ^{0.25} /g s	109400	
K_1	$8.06E+22 (N/m^2)^2$	220200	1.20E+23 (N/m ²) ²	223065	
K_2	1.41E-02	-37320	1.77E-02	-36582	
K_3	$1.14E+25 (N/m^2)^2$	182400	2.12E+21 (N/m ²) ²	186483	
$K_{\mathrm{CH_{4}}}$	6.65E-09 (N/m ²) ⁻¹	-38280			
$K_{\mathrm{H}_2\mathrm{O}}$	1.77E+05	-88680	9.25E+00	15900	
K_{H_2}	6.12E-14 (N/m ²) ⁻¹	-82900	1.80E-11 (N/m ²) ^{-0.5}	-93400	
K _{CO}	8.23E-10 (N/m ²) ⁻¹	-70650	5.13E-16 (N/m ²) ⁻¹	-140000	

B4. Figures for process simulation

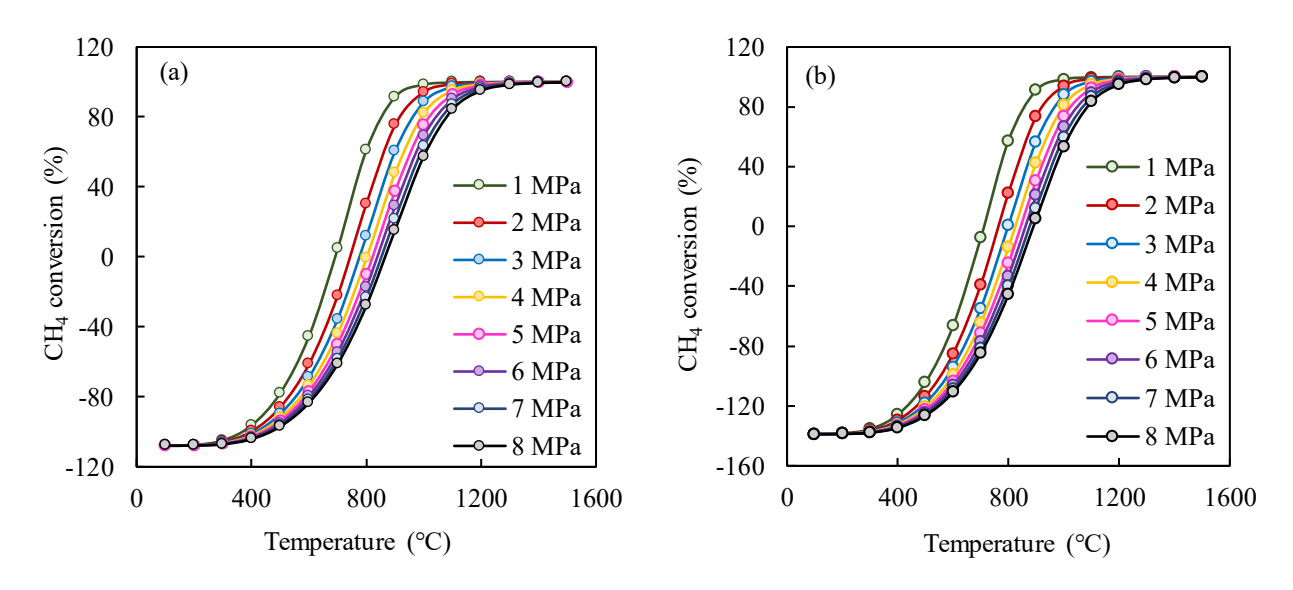


Fig. 1B: Impact of temperature and pressure on methane conversion: (a) Adjuna gas and (b) Uthmaniyah gas.

Supplementary C: Molecular dynamic simulation

C1. MD simulation method

The Large-scale Atomic/Molecular Massively Parallel Simulator (LAMMPS) was employed due to its robustness in performing molecular dynamic (MD) simulations with high computational efficiency and its ability to handle complex interactions in large atomic systems (Raza et al., 2022). In this study, LAMMPS was used to simulate gas diffusion in graphite under controlled conditions. To ensure stability, the x and y dimensions were fixed while relaxation was allowed along the z-axis to maintain a low density of ~0.1 g/cm³. An NVT (constant Number of particles, Volume, and Temperature) ensemble simulation was subsequently performed under isothermal and isochoric conditions for 100

picoseconds with a time step of 1 femtosecond to equilibrate the system and achieve the target density. Both the NPT (constant Number of particles, Pressure, and Temperature) and NVT ensembles were regulated using a Nose-Hoover thermostat to ensure accurate temperature control during the simulations. Interatomic interactions were modeled using the Lennard-Jones potential for van der Waals forces and the Ewald summation for electrostatic interactions. Once equilibrium was reached and Brownian motion was observed after 1 ns, the self-diffusivity of gases was computed under a constant energy-constant volume ensemble using the MedeA diffusion module.

C2. Gas diffusivity by molecular simulation

The self-diffusivity of gases through graphite is investigated via molecular simulation study. From the molecular simulation studies, Knudsen number which depicts the gas flow regime through a porous medium was computed. The values were computed for H_2 and CO_2 through graphite at varying slits of pore sizes (i.e. 1 nm, 2 nm, 4 nm and 8 nm) across varying pressures (i.e. 2-21 MPa) at a constant temperature of 350 K. The Knudsen number varies from 0.13 to 6.3, showing that the predominant transport mechanism is transitional, which falls between slip flow and molecular flow. For self-diffusion studies, the effective diffusivity (D_{eff}) for both gases shows a decreasing trend with pressure irrespective of the slit-pore size which corroborates the experimental study (Fig. C1). Fig. C1 also shows that differences in D_{eff} for the gases are more pronounced at lower pressures as observed in the experimental study. Using the D_{eff} of the gases, averagely the graphite has an ideal separation factor $[\alpha (H_2/CO_2)]$ of 3.13 and 3.42 in 1 nm and 8 nm slit-pore respectively.

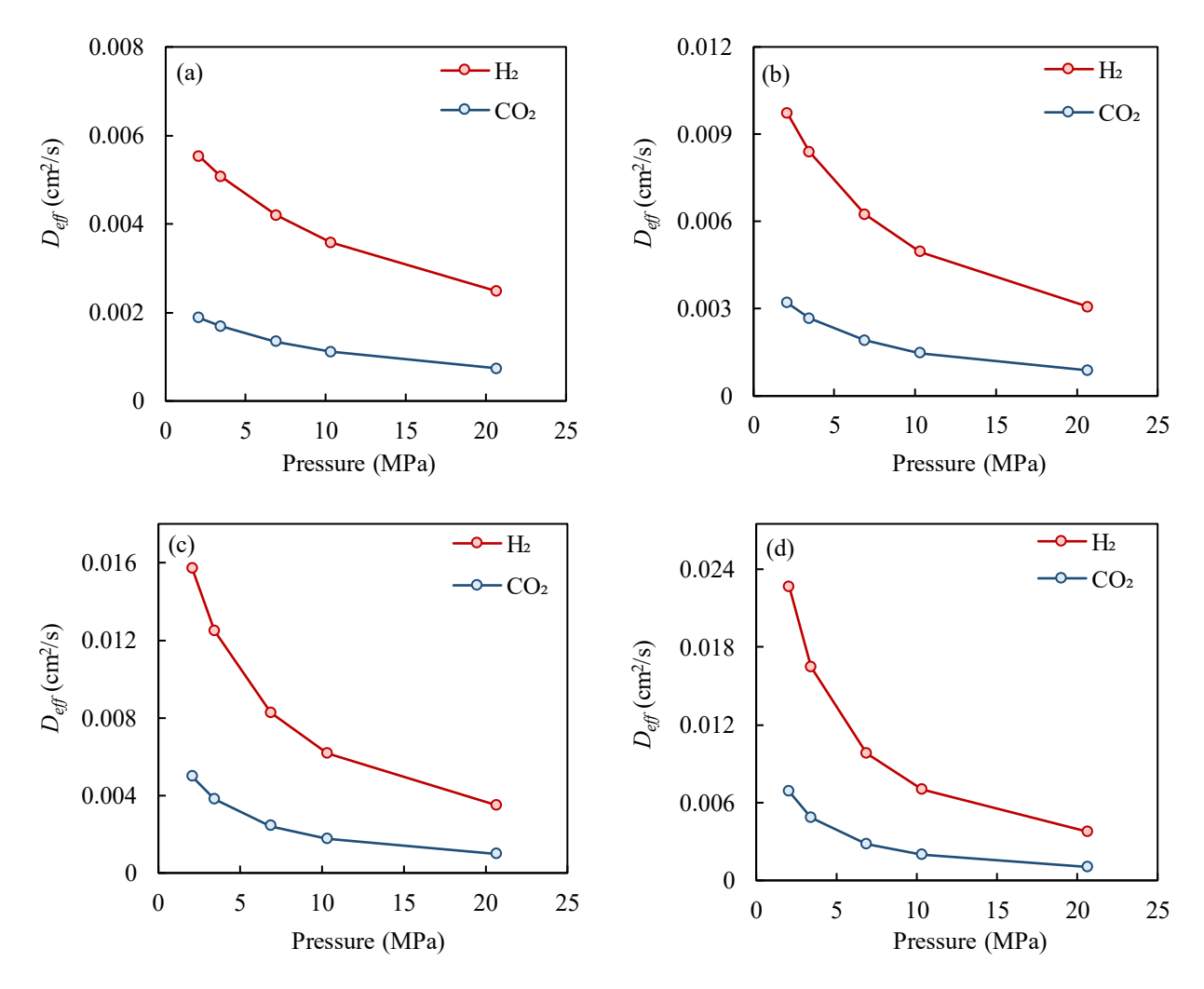


Fig. C1: Self diffusivity of H₂ and CO₂ through (a) 1 nm, (b) 2 nm, (c) 4 nm and (d) 8 nm slit-pore sizes.

Supplementary D: Pulse decay theory

The dimensionless pressure difference between the upstream and downstream cells is given by (Dicker & Smits, 1988):

$$\Delta p_D = \frac{p_u(t) - p_d(t)}{p_u(0) - p_d(0)} \tag{D1}$$

where t is time and $p_u(0)$ and $p_d(0)$ are the upstream and downstream pressures at the start of the experiment while $p_u(t)$ and $p_d(t)$ are the upstream and downstream pressures at any time. For minimal pressure changes (<5%), the late-time dimensionless differential pressure reduces to a single exponential function of time and may be approximated as:

$$ln(\Delta p_D) = ln(f_0) + s_1 t \tag{D2}$$

where f_0 is a constant and s_1 is the slope given as:

$$s_1 = -\frac{D\phi_e f_1 A \left(\frac{1}{V_u} + \frac{1}{V_d}\right)}{l} \tag{D3}$$

where D is gas diffusivity, ϕ_e is the effective porosity of the sample, l is sample length and A is the cross-sectional area of the sample. f_l is defined as:

$$f_1 = \frac{\theta_1^2}{a+b} \tag{D4}$$

where θ_1 is the first solution of the transcendental equation (Equation C5) while a and b denote the ratios of the sample's gas-storage capacity to those of the upstream and downstream cells, respectively (Equation C6):

$$\tan \theta = \frac{(a+b)\theta}{\theta^2 - ab} \tag{D5}$$

$$a = \frac{V_p(1 + f_a)}{V_u} \text{ and } b = \frac{V_p(1 + f_a)}{V_d}$$
 (D6)

where f_a accounts for gas adsorption. Therefore, f_a is zero when no adsorption occurs and a and b become the volume ratios between the sample and the cells. From the pressure pulse decay data recorded, Δp_D can be computed and plotted as a semi log against time. The late-time segment is linear, and its slope s_I is obtained by least-squares fitting. The gas diffusivity is then evaluated via the rearranged form of Equation C3:

$$D = -\frac{s_1 l}{\phi_e f_1 A \left(\frac{1}{V_U} + \frac{1}{V_d}\right)} \tag{D7}$$

References

- Afanasev, P., Smirnov, A., Ulyanova, A., et al. Experimental study of catalytically enhanced cyclic steam-air stimulation for *in situ* hydrogen generation and heavy oil upgrading. Catalysts, 2023, 13(8), 1172.
- Al-Malah, K. I. M. Aspen Plus: Chemical Engineering Applications. Hoboken, New Jersey, John Wiley & Sons, 2022.
- Askarova, A., Afanasev, P., Popov, E., et al. Application of oil *in situ* combustion for the catalytic methane conversion in the porous medium of the gas reservoir. Journal of Petroleum Science and Engineering, 2023, 220, 111256.
- Atsumi, H., Tauchi, K. Hydrogen absorption and transport in graphite materials. Journal of Alloys and Compounds, 356, 2023, 705–709.
- Bartolomei, M., Giorgi, G. A novel nanoporous graphite based on graphynes: first-principles structure and carbon dioxide preferential physisorption. ACS Applied Materials & Interfaces, 2016, 8(41), 27996–28003.
- He, H., Li, Q., Tang, J., et al. Study of hydrogen generation from heavy oil gasification based on ramped temperature oxidation experiments. International Journal of Hydrogen Energy, 2023, 48(6), 2161–2170.
- Ikpeka, P. M., Ugwu, J. O. *In situ* hydrogen production from hydrocarbon reservoirs—modelling study. RSC Advances, 2023, 13(18), 12100–12113.
- Kapadia, P. R., Kallos, M. S., Gates, I. D. Potential for hydrogen generation from *in situ* combustion of Athabasca bitumen. Fuel, 2011, 90(6), 2254–2265.
- Kapadia, P. R., Wang, J. J., Kallos, M. S., et al. Practical process design for *in situ* gasification of bitumen. Applied Energy, 2013, 107, 281–296.
- Mishra, A. K., Ramaprabhu, S. Study of CO2 adsorption in low cost graphite nanoplatelets. International Journal of Chemical Engineering and Applications, 2010, 1(3): 266-269.
- Okoji, A. I., Taiwo, A. E., Adeoye, J. B., et al. Process Integration of Hydrogen Production Using Steam Gasification and Water-Gas Shift Reactions: A Case of Response Surface Method and Machine Learning Techniques. International Journal of Energy Research, 2024, 2024(1): 6843951.
- Pu, W., Tang, X., Li, L., et al. Experimental investigation on *in-situ* hydrogen generation from depleted heavy oil reservoir by gasification. Petroleum Science and Technology, 2023, 42(25): 1-18.
- Raza, A., Alafnan, S., Glatz, G., et al. Hydrogen diffusion in organic-rich porous media: implications for hydrogen geo-storage. Energy & Fuels, 2022, 36(24): 15013-15022.
- Roussanaly, S., Anantharaman, R., Lindqvist, K. Multi-criteria analyses of two solvent and one low-temperature concepts for acid gas removal from natural gas. Journal of Natural Gas Science and Engineering, 2014, 20: 38-49.
- Schneider, R., Rai, A., Mutzke, A., et al. Dynamic Monte-Carlo modeling of hydrogen isotope reactive-diffusive transport in porous graphite. Journal of Nuclear Materials, 2007, 367: 1238-1242.
- Schulz, A., Steinbach, F., Caro, J. Pressed graphite crystals as gas separation membrane for steam reforming of ethanol. Journal of Membrane Science, 2014, 469: 284-291.
- Song, P., Li, Y., Yin, Z., et al. Simulation of hydrogen generation via *in-situ* combustion gasification of heavy oil. International Journal of Hydrogen Energy, 2024, 49, 925–936.
- Song, P., Li, Y., Yin, Z., et al. Hydrogen generation from heavy oils via *in-situ* combustion gasification. Paper SPE-212986-MS Presented at the SPE Western Regional Meeting, Anchorage, Alaska, USA, 22-25 May, 2023.
- Spitsyn, A., Pisarev, A., Skovoroda, A., et al. Permeation of hydrogen through MPG-8 graphite. Journal of Nuclear Materials, 2007, 363: 833-838.

- Spitsyn, A. V, Golubeva, A. V, Mayer, M., et al. Gas-driven hydrogen isotopes permeation through different carbon materials. Journal of Nuclear Materials, 2009, 390: 701-704.
- Trinh, T. T., Vlugt, T. J. H., Hägg, M. -B., et al. Selectivity and self-diffusion of CO2 and H2 in a mixture on a graphite surface. Frontiers in Chemistry, 2013, 1: 38.
- Żogała, A. Critical analysis of underground coal gasification models. Part I: equilibrium models-literary studies. Journal of Sustainable Mining, 2014b, 13(1): 22-28.